Materials Horizons

ROYAL SOCIETY OF CHEMISTRY

COMMUNICATION

View Article Online
View Journal | View Issue

Cite this: *Mater. Horiz.*, 2025, **12**, 9221

Received 28th May 2025,
Accepted 21st July 2025

DOI: 10.1039/d5mh01009h

rsc.li/materials-horizons

Tri-band smart window envelope based on temperature adaptive kirigami structure†

Tao Zhang,‡[ab] Zewei Shao,‡[ab] Cuicui Cao,[ab] Chengcong Li,[ab] Zhongshao Li,[ab] Fei Cao,[ac] Genshui Wang,[ac] John Bell,[d] Hongjie Luo,[e] Ping Jin[ab] and Xun Cao*[ab]

Regulating thermal radiation exchange between windows and the environment is crucial for building energy efficiency. While traditional low-emissivity (Low-E) windows and emerging smart windows offer promising solutions, they face challenges in adapting to complex changes in temperature and light conditions. In this paper, we introduce a temperature-adaptive radiator with a kirigami structure (TARK) window envelope, which integrates a vanadium dioxide (VO_2) based Fabry–Pérot (F–P) cavity with an angle-adjustable kirigami structure. This design enables temperature-adaptive solar modulation and angle-adjustable thermal radiation, addressing the limitations of conventional approaches. Specifically, the TARK achieves 31.10% solar modulation (ΔT_{SOL}), 0.96 mid-infrared emissivity (ε_{MIR}) at high temperatures, and 0.63 mid-infrared modulation ($\Delta\varepsilon_{MIR}$) with angle-adjustable radiation capabilities. Experimental validation under indoor and outdoor conditions confirms its directional radiation performance and robustness across diverse weather scenarios. Moreover, the device demonstrates up to 25.3% savings in HVAC energy consumption compared to glass, highlighting its potential for significant energy savings in building applications. This work advances the development of next-generation smart window technologies by combining materials science, structural engineering, and environmental adaptability.

New concepts

Windows are vital for providing natural light and thermal insulation in buildings but remain among the least energy-efficient components, with their thermal radiation regulation historically neglected. In this work, we present a rationally designed flexible membrane system and a mechanically structured temperature-adaptive radiator with a kirigami structure (TARK), which achieves tri-band modulation through the phase transition of vanadium dioxide and mechanical structural stretching while controlling the directional angle of thermal radiation *via* mechanical structure deflection, enabling the device to adapt to complex environments. The TARK shows remarkable mechanical stability and high modulation performance, with a solar modulation rate of 31.10% and an emissivity modulation rate of 0.63. Compared with existing advanced smart window technologies, the TARK maintains high modulation performance while enabling angle-selective control of thermal radiation. Its energy-saving benefits have been demonstrated in various climate zones globally. In 23 regions, the TARK can save up to 171.9 MJ m^{-2} of energy per year, with an average saving of 89.5 MJ m^{-2}, which is about 16.0% lower than that of conventional glass. This study provides a new method for developing energy-efficient window technologies by combining material phase changes and dynamic mechanical design for thermal regulation.

1. Introduction

Windows serve as the primary interface for energy exchange between indoor and outdoor environments in building systems.[1–7] These transparent envelopes facilitate solar radiation transmission across multiple spectra: visible light (VIS, 380–780 nm) for daylighting and heat capture, and near-infrared (NIR, 780–2500 nm) for solar heat gain, while simultaneously enabling mid-infrared (MIR, 8–13 μm) radiative cooling through thermal emission.[3,8] To reduce building energy consumption and enhance lighting utilization efficiency under complex environmental conditions, comprehensive optimization of the spectrum spanning visible to infrared wavelengths is essential.

Driven by this demand, thermochromic materials[2,5,9–17] have been extensively investigated for their temperature-adaptive properties. Vanadium dioxide (VO_2) and hydrogels are two of the most widely studied thermochromic window

[a] State Key Laboratory of High Performance Ceramics and Superfine Microstructure, Shanghai Institute of Ceramics, Chinese Academy of Sciences, Shanghai, 200050, China. E-mail: cxun@mail.sic.ac.cn
[b] Center of Materials Science and Optoelectronics Engineering, University of Chinese Academy of Sciences, Beijing, 100049, China
[c] The Key Lab of Inorganic Functional Materials and Devices, Shanghai Institute of Ceramics, Chinese Academy of Sciences, Shanghai 200050, China
[d] Office of the Deputy Vice-Chancellor (Research and Innovation), Research and Innovation Division, University of Southern Queensland, Toowoomba, Queensland, Australia
[e] Institute for the Conservation of Cultural Heritage, Shanghai University, Shanghai, China

† Electronic supplementary information (ESI) available. See DOI: https://doi.org/10.1039/d5mh01009h

‡ These authors contributed equally to this work.

materials, but the application of hydrogels has been limited by challenges in encapsulation and their high haze under high-temperature conditions. VO_2 is widely recognized as a prototypical thermochromic material, exhibiting exceptional thermal radiation management capabilities due to its near-room-temperature phase transition and wide-range emissivity modulation. However, when VO_2 thin films are integrated with a Fabry–Pérot (F–P) cavity to achieve tunable emissivity, the bottom metal layer imposes significant constraints on optical modulation across both the visible and near-infrared spectral regions.[18] Additionally, the inherent low visible light transmittance of VO_2 complicates achieving high solar modulation efficiencies.[1] Moreover, most current VO_2 thin films are fabricated on rigid substrates, which limits their applicability in flexible or adaptive systems.[19]

Meanwhile, in practice, energy-efficient windows are always tilted or shaded, which reduces their cooling performance compared to horizontal settings.[20] Therefore, for windows, especially in high-rise buildings with a large number of glazed facades, controlling the radiation angle is important to improve the energy exchange between the window and the environment. In recent years, leveraging gradient epsilon-near-zero (ENZ) materials,[21–25] microstructures,[26–33] and Brewster effect[34] to control the directionality of thermal radiation have become a prominent research frontier. However, their intricate fabrication processes impose substantial constraints on their practical applications. Using macrostructures to direct thermal radiation is a proven solution,[35,36] but a fixed radiation angle is incompatible with complex and changing weather conditions. In the case of windows, adding an extra envelope is a simpler and more effective energy-saving method.[37,38] The kirigami structure has been innovatively used to dynamically switch the thermal radiation angle due to its simple structure with excellent shape programming and reconfigurability.[4,39–42] However, the structure lacks an adaptive adjustment mechanism for intelligent environmental response, and controlling the radiation angle remains a significant challenge given the requirements for visibility and scalability of the window.

Here, we propose the design of a temperature adaptive radiator with a kirigami structure (TARK) that integrates a kirigami structure with a flexible VO_2 film based F–P cavity. This device achieves tri-band spectral modulation and adjustable omni-directional thermal radiation angles in vertical windows through mechanical stress and temperature variations, demonstrating adaptive energy-saving potential in varying climate regions. The experimental results indicate that the device is capable of modulating up to 0.63 in the 8–13 μm range ($\Delta\varepsilon_{MIR}$) and 31.10% in the solar spectral range (ΔT). Simulations show that the TARK can save up to 25.3% of HVAC energy compared to ordinary glass in buildings in 22 regions worldwide, while still meeting interior lighting requirements.

2. Results and discussion

2.1. Design of the tri-band TARK envelope

Drawing on the solar spectrum and the atmospheric window, we propose a set of ideal energy-saving window characteristics (Fig. 1a) designed to optimise the utilization of tri-band radiation across the VIS, NIR, and MIR regions. For the bright heating mode, high solar transmittance (T_{SOL}) and low MIR emissivity (ε_{MIR}) are critical, enabling solar energy to effectively heat the interior while minimizing radiative heat loss to the external environment. The bright cooling mode prioritizes high visible transmittance (T_{VIS}) to meet enhanced lighting requirements, coupled with elevated ε_{MIR} to promote additional radiative cooling. Conversely, the dark cooling mode achieves low T_{SOL} and high ε_{MIR} at elevated temperatures while preserving adequate T_{VIS} to balance light transmission and cooling efficiency. The detailed modulation strategy of the TARK system is depicted in Fig. 1b. In bright heating mode, the stretched structure, combined with the insulating VO_2 (I) phase (brown layer), allows both VIS and NIR radiation to penetrate the interior, while the downward-oriented bridge structure inhibits radiative cooling through the thermal reflector (red layer). This design mitigates heat loss, as effective radiative cooling is challenging for emitters not directly exposed to outer space.[30] In bright cooling mode, the stretched structure continues to facilitate VIS transmission into the room; however, the metallic VO_2 (M) phase (yellow layer) partially blocks NIR, and the upward-oriented bridge structure enhances cooling by directing thermal radiation outward from the window to meet additional cooling demands. By contrast, the closed structure in dark cooling mode minimizes T_{SOL} while retaining a moderate level of T_{VIS}. Furthermore, its high emissivity at elevated temperatures reduces the energy required for cooling.

Fig. 1c illustrates the application scenarios for these three modes. The bright heating mode, suited for cold winter conditions, maximizes solar irradiance transmission while suppressing radiative cooling from the window. The bright cooling mode, optimised for hot summer environments, ensures sufficient daylight penetration while addressing additional cooling needs. Meanwhile, the dark cooling mode, also applicable in bright summer conditions, blocks most solar irradiance but preserves partial visible transmittance for daylighting, achieving an adaptive high-emissivity surface to enhance radiative cooling. Fig. 1d depicts the switching processes between cooling modes (bright cooling and dark cooling) and the heating mode. The phase transition of VO_2 (I) into VO_2 (M) creates temperature-adaptive emissivity while preserving visible transparency, and divides the device into a high temperature state and a low temperature state. On the other hand, mechanical switching in combination with thermochromics can further provide a variety of modes.

2.2. Characterization of the tri-band TARK envelope

Based on the TARK structure described in the previous section, the system can be partitioned into two functional components: the passive regulation component (F–P cavity) and the mechanical switching component (kirigami structure), as illustrated in Fig. 2a. To achieve a balance between the regulatory performance of the cavity and the mechanical stretchability of the overall structure, we employed transparent and highly stable polyimide (TPI) as the substrate to support both the F–P cavity and the kirigami structure. Detailed properties of the TPI are provided in Fig. S1 (ESI†).

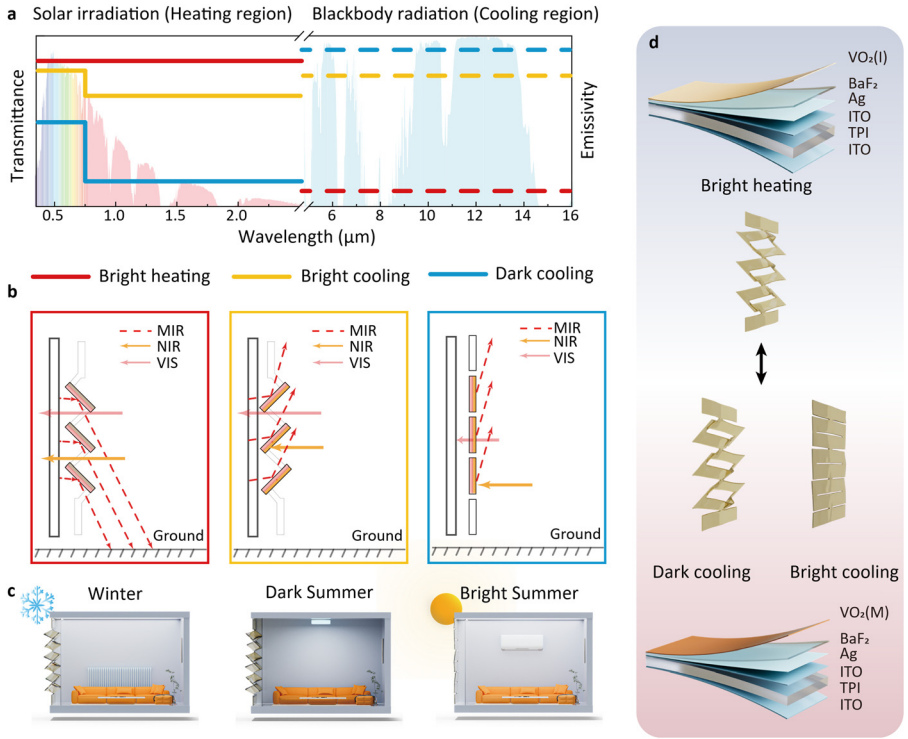

Fig. 1 The TARK thermal co-regulation strategy. (a) Ideal spectra for dynamic windows, which regulate the solar spectrum and MIR radiation among bright heating, bright cooling and dark cooling modes. (b) Detailed working principles of the TARK, VIS, NIR and MIR are represented using three different arrows. Consistent with the spectrum, in bright heating mode, high T_{SOL} and low ε_{MIR} are paramount, allowing the sun to heat the room while mitigating radiative cooling to the outside; the bright cooling mode balances high T_{VIS} for enhanced light needs with high ε_{MIR} for additional cooling effects; the dark cooling mode achieves low T_{SOL} and high ε_{MIR} at high temperatures while maintaining T_{VIS}. (c) Applicable scenarios, including winter, dark summer and bright summer. (d) Schematic of TARK switching modes at low temperatures (bright heating mode) and high temperatures (dark cooling and bright cooling).

For the F–P cavity, a switchable sandwiched structure of VO_2/BaF_2/Ag–ITO is used to realize on/off modulation of MIR absorption. VO_2 acts as a switchable cavity mirror: at low temperatures, VO_2 in the insulating phase allows high MIR transmittance; at high temperatures, VO_2 in the metallic phase exhibits high reflectance to activate the F–P cavity.[11] BaF_2, with its high transmittance in the MIR range, serves as a transparent spacer between the top VO_2 layer and the bottom metal reflective layer.[12] To balance high MIR reflectivity and visible transmittance, Ag–ITO is employed as the bottom MIR mirror (detailed ITO and Ag–ITO optical properties are shown in Fig. S2, ESI†). The inner side of the device is a thicker ITO layer to ensure sufficient MIR reflectivity (see Fig. S3, ESI†). Notably, the mechanical structure can be fabricated using a knife (Fig. S4, ESI†), and the cutting has a negligible effect on the film properties (Fig. S5, ESI†).

To systematically explore the relationship between $\Delta\varepsilon_{MIR}$ and layer thicknesses, we performed optical simulations to optimise thermal performance. As depicted in Fig. 2b, a $\Delta\varepsilon_{MIR}$ mapping was generated by fixing the Ag/ITO reflective layer thickness at 180 nm while systematically varying the VO_2 (10–60 nm) and BaF_2 (800–2000 nm) thicknesses. The results indicate that optimal performance is achieved when the BaF_2 thickness ranges from 1200 to 1600 nm and the VO_2 thickness is between 20 and 40 nm. Fig. S6 (ESI†) shows that as the BaF_2 thickness increases (1000–1600 nm), the peak wavelength exhibits a redshift, whereas the peak amplitude decreases with increasing VO_2 thickness.

Guided by the simulation results, we fabricated VO_2/BaF_2/Ag/ITO multilayers with the corresponding thicknesses. Detailed materials characterization of the multilayers, including XPS, XRD, and AFM, can be found in Fig. S7–S9 (ESI†). The ε_{MIR} of the prepared samples was measured as shown in Fig. S10 (ESI†), and we then obtained the $\Delta\varepsilon_{MIR}$ values of the samples (marked in Fig. 2b) at low and high temperatures. The highest $\Delta\varepsilon_{MIR}$ (0.63) was achieved with a 1400 nm BaF_2 layer and a 40 nm VO_2 layer; the cross-sectional SEM image and corresponding EDS line scan are shown in Fig. 2c.

For the kirigami structure, controlled transverse bending deformation can be achieved by axially stretching the device. Applying different stresses to lift or lower one end of the structure results in faceted deformation at varying structure angles (θ) in different directions. To assess the impact of the TRAK envelope angle on window radiation, we simulated the angularly distributed emissivity at a wavelength of 10 μm using the simplified model in Fig. S11 (ESI†). As depicted in Fig. 2d, the thermal radiation from the simplified model exhibits a strong angular correlation, with most of the thermal emission confined within a 30° range. In particular, the sample with θ = 45° can redirect the thermal radiation from the window.

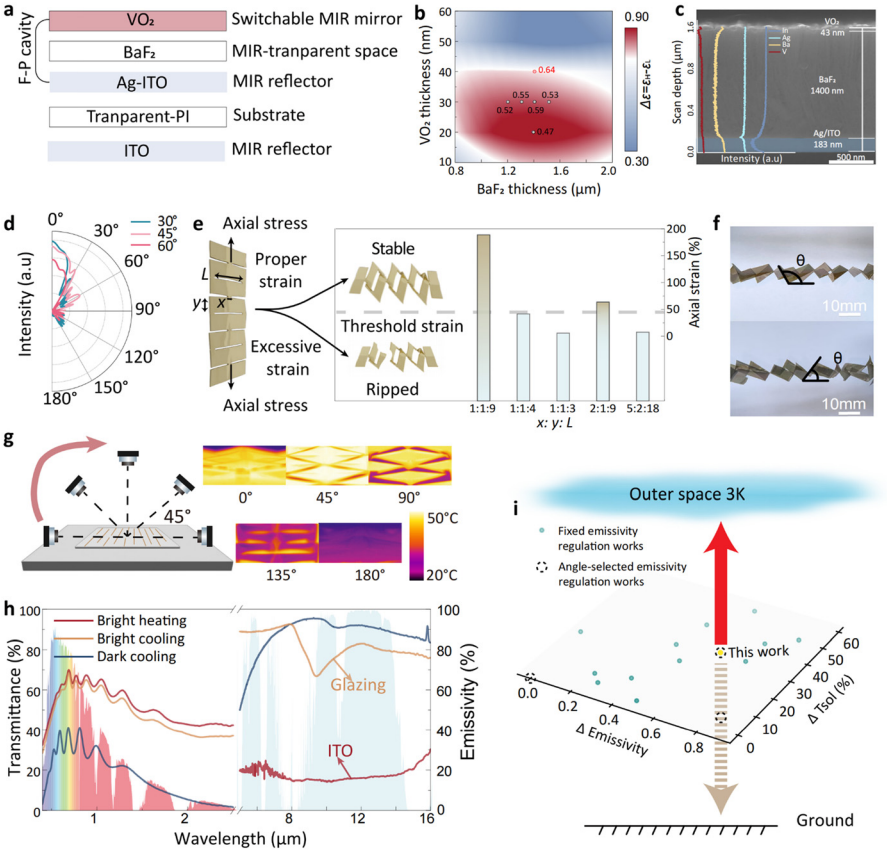

Fig. 2 Characterization of the tri-band TARK envelope. (a) Schematic of the multi-layer TARK structure. (b) Mapping results of $\Delta\varepsilon_{MIR}$ with varied thicknesses of VO_2 and BaF_2 layers, where the thickness of bottom ITO/Ag was fixed at 180 nm. The special symbols in the figure represent the $\Delta\varepsilon_{MIR}$ of the actual prepared samples. (c) Cross-sectional SEM image of the TARK films and the corresponding EDS line scan. (d) Simulated angle-dependent emission intensity distribution. (e) The strain behaviour of the TARK samples at different cutting ratios (x, y, L) is above the threshold strain (*i.e.* stable up to 45°) only for (x, y, L = 1 : 1 : 9) and (x, y, L = 2 : 1 : 9). (f) Photographs of the samples achieving the angular response (scale bar, 10 mm). (g) Experimental setup for examining the samples' surface temperatures on a hot stage and thermal images of the TARK envelope at different observation angles, revealing directional thermal radiation. (h) Solar spectral transmittance TARK films in bright heating, bright cooling and dark cooling modes, adaptive emissivity surface at high temperatures, thermal radiation emitter glass, and thermal radiation reflector ITO, in the mid-far infrared demonstrating high tri-band modulation. (i) The modulation capability comparison between different similar works.[2–5,11,13,18,22,39,45–49] This work demonstrates angle-selective emissivity while retaining high values for both ΔT_{SOL} and $\Delta\varepsilon_{MIR}$.

The kirigami structure must meet thermal radiation modulation design requirements and maintain mechanical stability during repetitive deformations. The geometrical parameters include transverse cut length L, transverse cut spacing x and axial layer spacing y, as shown in Fig. 2e. The simplified geometric truss structure is shown in Fig. S14 (ESI†), where eqn (1) was used to predict the rotational angle of feature points under high strain.[43,44]

$$\theta = \cos^{-1}\left(\frac{1}{\varepsilon_A + 1}\right) \quad (1)$$

ε_A indicates the axial strain after stretching (more details can be found in Note S1, ESI†). A simple calculation indicates the required strain of 41.1% (threshold strain) at a θ of 45°. As shown in Fig. 2e, the device needs to maintain mechanical stability without ripping under threshold strain. Among the tested samples, only $x:y:L$ = 1 : 1 : 9 exhibited a strain significantly higher than the minimum threshold required to guarantee tensile stability. Consequently, $x:y:L$ = 1 : 1 : 9 was selected to determine the optimal cut ratio for the TARK structure. Photographs of the samples achieving the angular response after stretching are shown in Fig. 2f.

Fig. 2g presents the experimental setup for analyzing the surface temperatures of samples on a hot stage and the apparent temperature of a stretched envelope at different observation angles. Infrared images transition from yellow (warm) to purple (cool) as the angle increases. At small angles, exposed openings allow unobstructed thermal radiation (yellow), while larger angles obscure these areas, blocking radiation (violet). Uneven coloration stems from the film's variable fit on curved glass. Fig. S15 (ESI†) displays IR images of Low-E glazing, standard glass, and the TARK dark cooling mode at high and low temperatures. After stabilization, Low-E glazing consistently shows low emissivity, glass exhibits high emissivity, and the TARK shifts from resembling Low-E glazing below its phase transition temperature to matching glass above it, indicating a clear emissivity change.

Spectral response is achieved, as shown in Fig. 2h. At high temperatures in the unstretched state, T_{VIS} is 30.71% and T_{SOL} is 25.38%. Upon mechanical stretching, these values increase

significantly to T_{VIS} = 54.08% and T_{SOL} = 53.50%. At low temperatures in the stretched state, T_{VIS} reaches 56.80% and T_{SOL} reaches 56.47%. Additionally, the highest emissivity within the atmospheric window range is 0.96, with an adaptive $\Delta\varepsilon_{MIR}$ of 0.63. Besides, glass, acting as a thermal emitter, shows ε_{MIR} = 0.81, while ITO, functioning as a thermal reflector, shows ε_{MIR} = 0.15. As demonstrated in Fig. 2i and Table S1 (ESI†), compared to traditional VO_2 based F–P cavities used in smart windows, the proposed TARK demonstrates significantly higher modulation efficiency in the MIR, while also offering unique tri-band modulation and angle selectivity.[2,11,18] In contrast to smart windows that rely solely on kirigami structures, TARK offers adaptive dynamic modulation performance.[4,39] Furthermore, relative to other smart windows (such as electrochromic devices and thermochromic hydrogels),[5,9,45] the TARK's angular selectivity enables superior adaptability and functionality in more complex and variable environments.

2.3. Performance evaluation of the tri-band TARK envelope

Fig. 3a illustrates the experimental equipment for evaluating directional thermal radiation. We placed samples on top of a polymethyl methacrylate (PMMA) box covered with aluminium foil, with a liquid nitrogen-cooled heat sink simulator (foam box covered by black aluminium tape) positioned at the base. A temperature recorder was used to log the sample temperature variations over a several-hour period. Previous studies have demonstrated that different incident angles (θ) can modulate the direction of thermal radiation emission. To further validate this directional control effect, a proof-of-concept experiment was conducted in a laboratory setting, providing empirical evidence for the theoretical predictions.

Experimental results in Fig. 3b describe the working principles of these three modes. The dark cooling mode can maintain the temperature inside the chamber, due to the low emissivity of inner and outer sides isolating the radiative heat exchange between the sample and the environment, the maximum temperature difference (ΔT) is 1 °C compared to the glass. The bright heating mode achieves a 0.8 °C temperature increase compared to the glass, and the bridge structure suppresses radiation to the heat sink and replaces it with heat exchange between the top of the PMMA box and the sample. In the bright cooling mode, the bridge structure promotes thermal radiation exchange between the sample and heat sink by exposing more window to the heat sink, resulting in the lowest temperatures, with a maximum temperature drop of 0.4 °C compared to the glass, and a temperature drop of 0.6 °C relative to the bright heating mode. Such an indoor test is not sufficient to perfectly demonstrate the actual use of each mode, as not only complex weather conditions cannot be taken into account, but also the transmission characteristics of atmospheric windows and the ultra-low temperatures of outer space cannot be accurately replicated. However, the indoor test demonstrates objective results, with the bright cooling mode and bright heating mode showing directional radiation transmission

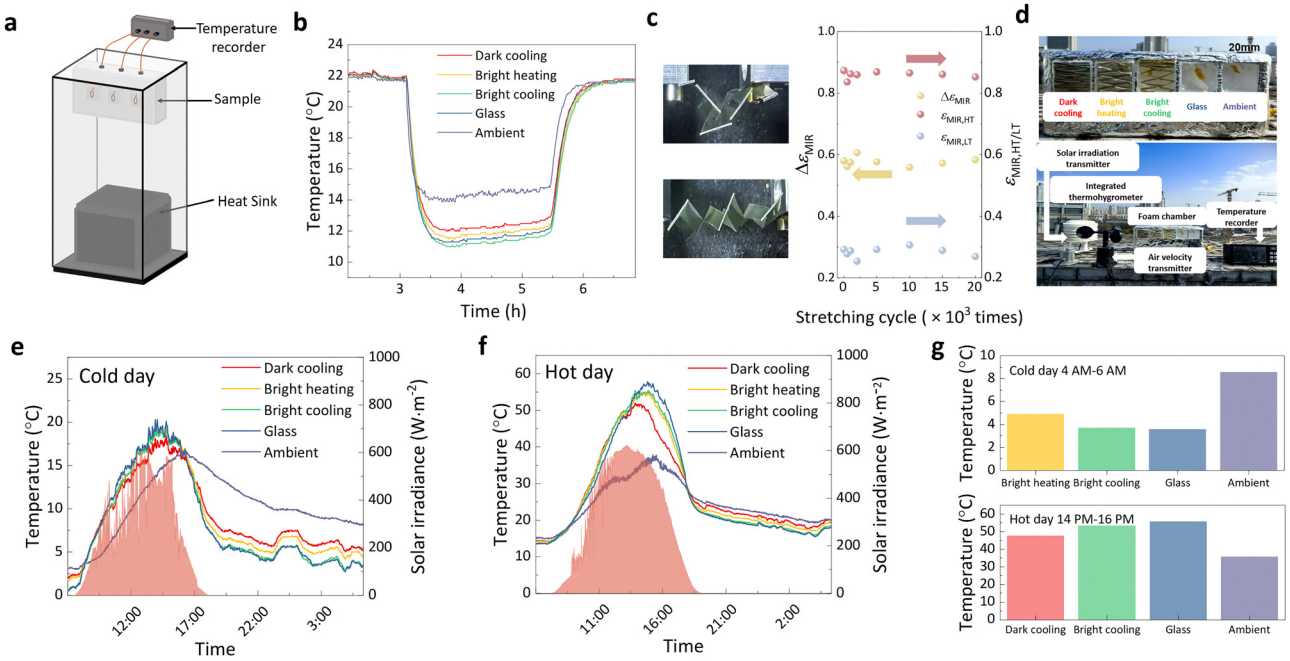

Fig. 3 Performance evaluation of the tri-band TARK envelope. (a) Proof-of-concept test model, heat sink at the base for simulating low temperatures in outer space and (b) experimental results, demonstrating directional radiation transmission characteristics, including the temperature of the four samples and ambient temperature. (c) Stretching cycle test; the left photographs show the stretching cycle process, while the right image shows the test results. The high-temperature emissivity ($\varepsilon_{MIR,HT}$) and low-temperature emissivity ($\varepsilon_{MIR,LT}$) remained consistently stable. (d) Photographs of the measurement set-up on the rooftop in Shanghai, China. The four experimental samples: dark cooling, bright heating, and bright cooling modes, and glass (scale bar, 20 mm). Outdoor temperature results, (e) on a cold day in Shanghai, China (17th January 2025), and (f) on a hot day in Shanghai, China (1 March 2025). (g) Temperature comparison on 17 January 2025 at night from 4 AM to 6 AM. Test results on 1 March 2025 at 14–16 PM.

characteristics. Furthermore, as shown in Fig. 3c, during the stretching cycle test, $\Delta\varepsilon_{MIR}$ did not exhibit a significant decrease even after 20 000 cycles. This result demonstrates the excellent mechanical stability of the TARK.

Then, we conducted outdoor tests on a rooftop in Shanghai, China to investigate the performance of the TARK under real outdoor conditions (Fig. 3d). Four samples – dark cooling, bright cooling, and bright heating modes and glass – were simultaneously monitored under natural weather fluctuations. Five temperature profiles as well as the intensity of the solar irradiation on hot/cold days were recorded as shown in Fig. 3e and f; as expected, different modes are suitable for different weather conditions.

Specifically, on a cold day (Fig. 3e), thermal regulation performance exhibits distinct mode-dependent characteristics. At midday, the temperature of dark cooling mode is lowest, with a maximum ΔT of 2.2 °C compared to glass *via* blocking of sunlight. Additionally, enhanced solar transmittance in bright cooling and bright heating modes raises the indoor temperature by 1.5–1.7 °C compared to the dark cooling mode, validating their passive heating capability. At lower solar irradiation intensities (<100 W m^{-2}), the bright cooling mode, due to the ability to emit thermal radiation directionally towards the sky, achieves near-glass equivalent temperatures, while the bright heating mode is 1.1 °C higher than glass on average by suppressing radiative cooling. As shown in Fig. 3g, on the cold day, bright heating exhibited temperature increases of 1.2 °C and 1.3 °C relative to bright cooling and glass, respectively, during the nighttime from 4:00 AM to 6:00 AM, based on average calculations.

On a hot day (Fig. 3f), when solar irradiation decreases, the overall trend is similar to that of the previous sunny winter. At midday, bright heating and bright cooling modes exhibit 7.1–8.1 °C higher temperature than the dark cooling mode due to the controlled T_{SOL}. The maximum indoor temperature of the glass sample is 57.8 °C, while the maximum indoor temperature of the dark cooling mode is only 51.9 °C, demonstrating excellent cooling capacity, with the maximum ΔT = 11.7 °C. Also in Fig. 3g, on the hot day, at 14:00–16:00 in the afternoon, the average ΔT = 7.9 °C between the dark cooling mode and glass. These practical demonstrations confirm the TARK's ability to fit varying weather conditions, which is essential for high-rise applications where both thermal and visual comfort need to be optimised.

2.4. Energy-saving evaluation of the tri-band TARK envelope

To further assess the global energy-saving potential of the TARK, a commercial office building was used in the energy simulation, as shown in Fig. S21 (ESI†), with a wall-through ratio of 0.33 and a total floor area of 4982.19 m^2. The TARK was simplified as blinds for computational convenience (Fig. S22, ESI†), and the corresponding simulation data are presented in Table S2 (ESI†). Global energy performance simulations across 22 regions (categorized into 19 ASHRAE climate zones, Fig. 4a) demonstrate 6.2–25.3% energy savings compared to conventional glass systems. As shown in Fig. 4b, in the 22 cities

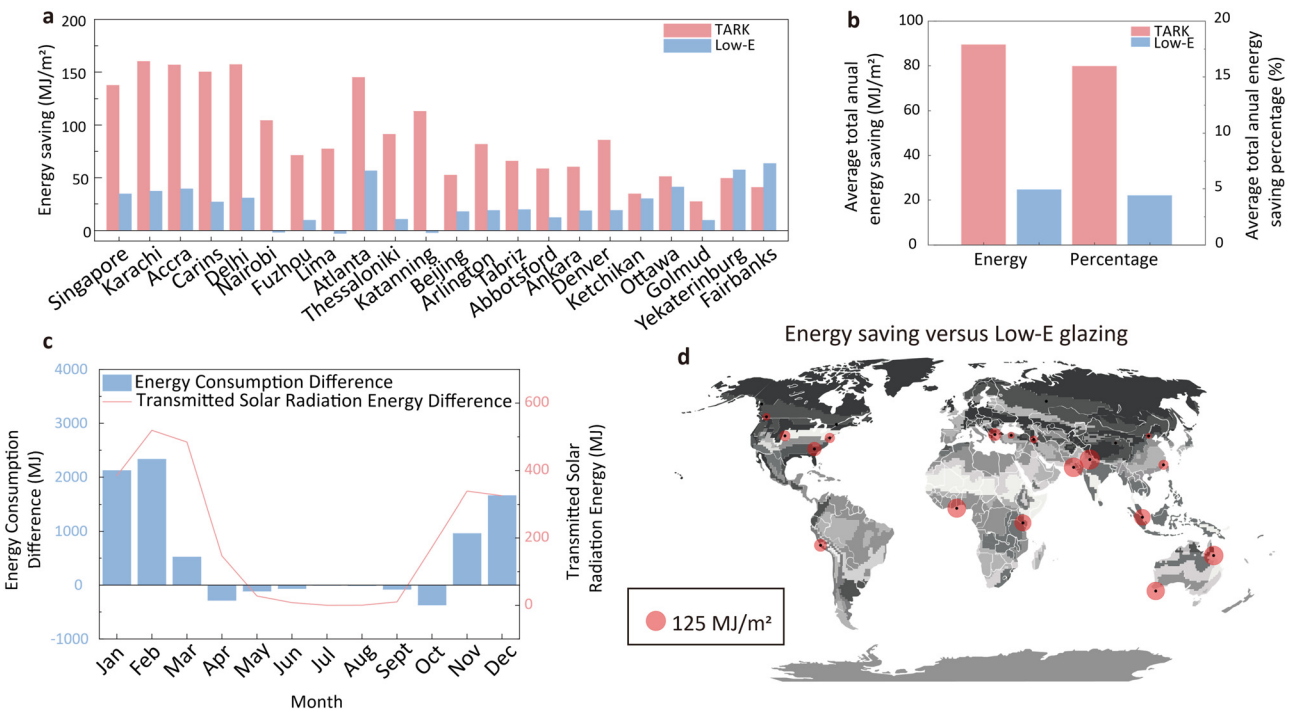

Fig. 4 Energy-saving evaluation of the tri-band TARK envelope. (a) Annual energy savings of the TARK and Low-E glazing *vs.* traditional glass in commercial buildings in different climate regions. (b) Average total energy savings of the buildings with the TARK and Low-E glazing compared to that using glass in representative cities of different climate zones. (c) Differences in energy consumption and solar radiation transmission energy through the window between the two modes and with the addition of mechanical switching. (d) Annual energy saving of the TARK compared to Low-E glazing.

mentioned above, the TARK saves an average of 89.5 MJ m^{-2} per year compared to glass, with an average energy saving of about 16.0%, and Low-E glazing saves about 24.7 MJ m^{-2} per year compared to glass, demonstrating the generalisability of the TARK. According to the calculations in Note S2 (ESI†), with an energy cost of 0.044 $$ per MJ, the average annual energy cost savings across all regions amount to 3.938 $$ per m^2. Furthermore, considering a grid electricity carbon emission factor of 0.094 kg CO_2 per MJ, the average annual carbon reduction is 8.413 kg m^{-2}. Fig. S23 (ESI†) compares the lighting energy consumption of the TARK with that of glass and Low-E glazing, which shows that the increase in lighting energy consumption due to the introduction of the TARK is negligible.

Later, to evaluate the significance of mechanical switching, we compared the three modes incorporating mechanical switching with the two modes without it (where the structure remains perpetually closed), as depicted in Fig. 4c. In Beijing, China, the addition of mechanical switching resulted in significant energy savings of about 6668.7 MJ for the whole year, with the highest increase in the window transmittance of solar radiation energy to 519.1 MJ, thus making effective use of solar energy. The above simulation demonstrates the advantages of adding mechanical switching. Although the device exhibits lower performance compared to Low-E glazing in high-latitude regions (Fairbanks, AK and Yekaterinburg, RU) where prolonged indoor heating relies heavily on solar transmission due to its reduced solar transmittance, it remains highly competitive across the other twenty evaluated regions, as shown in Fig. 4d. In practice, the TARK can be used in a variety of modes according to the actual situation to further improve energy efficiency.

3. Conclusion

The TARK we have developed combines a VO_2-based F–P cavity with a kirigami structure, achieving tri-band modulation with flexible adjustment in the MIR, NIR, and VIS ranges as well as the ability to switch the angles of omni-directional thermal radiation to adapt to complex and changing weather conditions. The unstretched state maintains T_{SOL} = 25.38%, while the stretched state enhances T_{SOL} to 53.50% at high temperatures. Meanwhile, the maximum emissivity in the MIR is 0.96 and the modulation rate is as high as 0.63. The device ultimately achieves efficient thermal management. Also, the stretched state preserves T_{VIS} > 50% for daylight utilization. The indoor test confirmed directional radiation control between the bright heating mode and bright cooling mode (ΔT = 0.6 °C). Meanwhile, outdoor tests demonstrated different modes are suitable for different weather conditions. At night, the bright cooling mode provides extra cooling *via* additional radiative cooling, while the bright heating mode maintains the room warm by suppressing thermal radiation. During the day, the dark cooling mode offers efficient cooling due to sun shading and adaptive high emissivity at high temperature, achieving ΔT = 11.7 °C compared with the glass sample. The bright cooling mode and bright heating mode, with their open structure, utilize solar irradiation for heating. Further energy saving simulations indicate that the TARK structure can save up to 25.3% of energy compared to glass in various global climate zones, demonstrating remarkably high potential for energy savings. Furthermore, the three modes of the TARK can be further tailored to enhance energy efficiency in practical scenarios, while the physical vapour deposition process for fabrication also ensures scalability.

4. Experimental section

Experimental details and characterization data are provided in the ESI.†

Author contributions

Xun Cao: conceptualization, funding acquisition, methodology, project administration, resources; Tao Zhang: conceptualization, methodology, investigation, writing (original draft), writing (review and editing), visualization; Zewei Shao: investigation, writing (review and editing), formal analysis, visualization; Cuicui Cao: conceptualization, investigation, writing (review and editing); Chengcong Li: formal analysis, writing (review and editing); Zhongshao Li: methodology, writing (review and editing); Fei Cao: formal analysis; Genshui Wang: formal analysis; John Bell: methodology; Hongjie Luo: methodology; Ping Jin: conceptualization, software.

Conflicts of interest

There are no conflicts to declare.

Data availability

All data needed to support the conclusions in the paper are presented in the paper and the ESI.† Additional data related to this paper may be requested from the corresponding author.

Acknowledgements

This study was financially supported by the National Key Research and Development Program of China (no. 2021YFA0718900), the National Natural Science Foundation of China (no. 62175248, 52302370, and U24A2061), Shanghai Science and Technology Funds (no. 23ZR1481900 and 25ZR1401373), and the Major Science and Technology Project of Yunnan Province (202302AB080023).

References

1 X. Li, C. Cao, C. Liu, W. He, K. Wu, Y. Wang, B. Xu, Z. Tian, E. Song, J. Cui, G. Huang, C. Zheng, Z. Di, X. Cao and Y. Mei, *Nat. Commun.*, 2022, **13**, 7819.
2 S. Wang, T. Jiang, Y. Meng, R. Yang, G. Tan and Y. Long, *Science*, 2021, **374**, 1501.

3 Z. Shao, A. Huang, C. Cao, X. Ji, W. Hu, H. Luo, J. Bell, P. Jin, R. Yang and X. Cao, *Nat. Sustainable*, 2024, **7**, 796.
4 H. Yin, X. Zhou, Z. Zhou, R. Liu, X. Mo, Z. Chen, E. Yang, Z. Huang, H. Li, H. Wu, J. Zhou, Y. Long and B. Hu, *Research*, 2023, **6**, 0103.
5 C. Lin, J. Hur, C. Y. H. Chao, G. Liu, S. Yao, W. Li and B. Huang, *Sci. Adv.*, 2022, **8**, eabn7359.
6 G. Lee, H. Kang, J. Yun, D. Chae, M. Jeong, M. Jeong, D. Lee, M. Kim, H. Lee and J. Rho, *Nat. Commun.*, 2024, **15**, 6537.
7 X. Zhao, A. Aili, D. Zhao, D. Xu, X. Yin and R. Yang, *Cell Rep. Phys. Sci.*, 2022, **3**, 100853.
8 J. Park, H. Lim, H. Keawmuang, D. Chae, H. Lee and J. Rho, *Small*, 2025, 2501840.
9 K. Wang, S. Liu, J. Yu, P. Hong, W. Wang, W. Cai, J. Huang, X. Jiang, Y. Lai and Z. Lin, *Adv. Mater.*, 2025, **37**, 2418372.
10 Y. Ke, Y. Yin, Q. Zhang, Y. Tan, P. Hu, S. Wang, Y. Tang, Y. Zhou, X. Wen, S. Wu, T. J. White, J. Yin, J. Peng, Q. Xiong, D. Zhao and Y. Long, *Joule*, 2019, **3**, 858.
11 C. Li, C. Cao, Z. Li, X. Ji, P. Jin and X. Cao, *Appl. Mater. Today*, 2024, **39**, 102297.
12 K. Tang, K. Dong, J. Li, M. P. Gordon, F. G. Reichertz, H. Kim, Y. Rho, Q. Wang, C.-Y. Lin, C. P. Grigoropoulos, A. Javey, J. J. Urban, J. Yao, R. Levinson and J. Wu, *Science*, 2021, **374**, 1504.
13 S. Liu, Y. Li, Y. Wang, Y. Du, K. M. Yu, H.-L. Yip, A. K. Y. Jen, B. Huang and C. Y. Tso, *Nat. Commun.*, 2024, **15**, 876.
14 J. Jin, J. Zhang, J. Zhang, X. Chen, S. Zou, Y. Xin, S. Liu, G. Liu, X. Yan and J. Huang, *Adv. Mater.*, 2025, **37**, 2416146.
15 S. So, J. Yun, B. Ko, D. Lee, M. Kim, J. Noh, C. Park, J. Park and J. Rho, *Adv. Sci.*, 2024, **11**, 2305067.
16 Y. Liu, Y. Tian, X. Liu, F. Chen, A. Caratenuto and Y. Zheng, *Appl. Phys. Lett.*, 2022, **120**, 171704.
17 P. Liu, S. Bae, J. Noh, M. Kim, J. W. Heo, D. Son, J. Kang, J. Rho, S. So, J. G. Kang and I. S. Kim, *ACS Appl. Electron. Mater.*, 2023, **5**, 5755.
18 S. Li, E. Yang, Y. Li, X. Mo, Z. Chen, Z. Zhou, G. Tao, Y. Long and B. Hu, *Nano Energy*, 2024, **129**, 110023.
19 C. Cao, B. Hu, G. Tu, X. Ji, Z. Li, F. Xu, T. Chang, P. Jin and X. Cao, *ACS Appl. Mater. Interfaces*, 2022, **14**, 28105.
20 J. Mandal, J. Anand, S. Mandal, J. Brewer, A. Ramachandran and A. P. Raman, *Cell Rep. Phys. Sci.*, 2024, **5**, 102065.
21 J. Xu, J. Mandal and A. P. Raman, *Science*, 2021, **372**, 393.
22 M. Bae, D. H. Kim, S.-K. Kim and Y. M. Song, *Nanophotonics*, 2024, **13**, 749.
23 B. Johns, S. Chattopadhyay and J. Mitra, *Adv. Photon. Res.*, 2022, **3**, 2100153.
24 Y. Ying, B. Ma, J. Yu, Y. Huang, P. Ghosh, W. Shen, M. Qiu and Q. Li, *Laser Photon. Rev.*, 2022, **16**, 2200018.
25 J. S. Hwang, J. Xu and A. P. Raman, *Adv. Mater.*, 2023, **35**, 2302956.
26 Z. Fan, T. Hwang, S. Lin, Y. Chen and Z. J. Wong, *Nat. Commun.*, 2024, **15**, 4544.
27 J. Yu, R. Qin, Y. Ying, M. Qiu and Q. Li, *Adv. Mater.*, 2023, **35**, 2302478.
28 J. Siegel, S. Kim, M. Fortman, C. Wan, M. A. Kats, P. W. C. Hon, L. Sweatlock, M. S. Jang and V. W. Brar, *Nat. Commun.*, 2024, **15**, 3376.
29 J. Zhou, T. G. Chen, Y. Tsurimaki, A. Hajj-Ahmad, L. Fan, Y. Peng, R. Xu, Y. Wu, S. Assawaworrarit, S. Fan, M. R. Cutkosky and Y. Cui, *Joule*, 2023, **7**, 2830.
30 F. Xie, W. Jin, J. R. Nolen, H. Pan, N. Yi, Y. An, Z. Zhang, X. Kong, F. Zhu, K. Jiang, S. Tian, T. Liu, X. Sun, L. Li, D. Li, Y.-F. Xiao, A. Alu, S. Fan and W. Li, *Science*, 2024, **386**, 788.
31 B. Ko, J. Noh, D. Chae, C. Lee, H. Lim, H. Lee and J. Rho, *Adv. Funct. Mater.*, 2024, **34**, 2410613.
32 Y. Ying, J. Yu, B. Qin, M. Zhao, T. Zhou, W. Shen, M. Qiu and Q. Li, *Laser Photon. Rev.*, 2023, **17**, 2300407.
33 C. Argyropoulos, K. Q. Le, N. Mattiucci, G. D'Aguanno and A. Alù, *Phys. Rev. B*, 2013, **87**, 205112.
34 Q. Chen, C. Li, X. Huang, Y. Lu, H. Xu, Y. An, L. Li, W. Li, X. Yin, X. Cao and D. Zhao, *Adv. Sci.*, 2025, **12**, 2416437.
35 P. Poredoš, H. Shan, C. Wang, Z. Chen, Z. Shao, F. Deng, H. Liu, J. Yu and R. Wang, *Energy Environ. Sci.*, 2024, **17**, 2336.
36 Q. Cheng, S. Gomez, G. Hu, A. Abaalkhail, J. E. Beasley, P. Zhang, Y. Xu, X. Chen, S. Tian, J. Mandal, A. P. Raman, N. Yu and Y. Yang, *Nexus*, 2024, **1**, 100028.
37 B. Svetozarevic, M. Begle, P. Jayathissa, S. Caranovic, R. F. Shepherd, Z. Nagy, I. Hischier, J. Hofer and A. Schlueter, *Nat. Energy*, 2019, **4**, 671.
38 W. Zou, Y. Wang, E. Tian, J. Wei, J. Peng and J. Mo, *Engineering*, 2024, **39**, 194.
39 S. Wang, Y. Dong, Y. Li, K. Ryu, Z. Dong, J. Chen, Z. Dai, Y. Ke, J. Yin and Y. Long, *Mater. Horiz.*, 2023, **10**, 4243.
40 T. Hirai, R. Iguchi, A. Miura and K. Uchida, *Adv. Funct. Mater.*, 2022, **32**, 2201116.
41 Y. Tang, G. Lin, S. Yang, Y. K. Yi, R. D. Kamien and J. Yin, *Adv. Mater.*, 2017, **29**, 1604262.
42 T.-H. Chen, Y. Hong, C.-T. Fu, A. Nandi, W. Xie, J. Yin and P.-C. Hsu, *PNAS Nexus*, 2023, **2**, 165.
43 A. Lamoureux, K. Lee, M. Shlian, S. R. Forrest and M. Shtein, *Nat. Commun.*, 2015, **6**, 8092.
44 J. Zhou, M. Liu, S. Wang, J. Zhang, M. Ni, S. Liu, Y. Wang, H. Deng, B. Liu and X. Gong, *Compos. B: Eng.*, 2024, **277**, 111368.
45 Y. Huang, S. Wu, S. Zhao, Z. Guo, Z. Zhao, X. Wu, B. Wang, F. Wang, A. Xi, F. Lan, Y. Li, J. Xu, R. Li, Y. Zhao and R. Zhang, *Energy Environ. Sci.*, 2025, **18**, 1824.
46 Y. Jia, D. Liu, D. Chen, Y. Jin, C. Chen, J. Tao, H. Cheng, S. Zhou, B. Cheng, X. Wang, Z. Meng and T. Liu, *Nat. Commun.*, 2023, **14**, 5087.
47 H. Zhang, X. Zhang, W. Sun, M. Chen, Y. Xiao, Z. Ding, D. Yan, J. Deng, Z. Li, J. Zhao and Y. Li, *Adv. Funct. Mater.*, 2024, **34**, 2307356.
48 Y. Jiang, Y. Wang, D. Kong, Z. Chen, Z. Yang, N. Cao, H. Chi, S. Zhu, Q. Zhang, J. Zhu and B. Zhu, *Natl. Sci. Rev.*, 2025, **12**, nwae408.
49 S. Wang, Y. Zhou, T. Jiang, R. Yang, G. Tan and Y. Long, *Nano Energy*, 2021, **89**, 106440.

